Check for updates

Advanced Electronic Materials

ADVANCED ELECTRONIC MATERIALS Open Access

www.advelectronicmat.de

RESEARCH ARTICLE OPEN ACCESS

Selective Tuning of Perpendicular Magnetic Anisotropy and Dzyaloshinskii–Moriya Interaction in Heterostructures Compatible with Magnetic Tunnel Junctions

Bob Vermeulen[1,2] | Seongbin Seo[3] | Domenico Giuliano[1,2] | Jyotirmoy Chatterjee[1] | Giacomo Talmelli[1] | Robert Carpenter[1] | Yann Canvel[1] | Yanan Li[1] | Björn Heinz[4] | Philipp Pirro[4] | Bart Sorée[1,5,6] | Kristiaan Temst[1,2] | Van Dai Nguyen[1] | Gouri Sankar Kar[1] | Siddharth Rao[1]

[1]IMEC, Leuven, Belgium | [2]Department of Physics and Astronomy, Quantum Solid-State Physics (QSP) Division, Katholieke Universiteit Leuven, Leuven, Belgium | [3]Department of Physics, University of Ulsan, Ulsan, Republic of Korea | [4]Fachbereich Physik and Landesforschungszentrum OPTIMAS, Rheinland-Pfälzische Technische Universität Kaiserslautern-Landau, Kaiserslautern, Germany | [5]Department of Electrical Engineering, ESAT-INSYS Division, Katholieke Universiteit Leuven, Leuven, Belgium | [6]Department of Physics, Universiteit Antwerpen, Antwerp, Belgium

Correspondence: Bob Vermeulen (bob.vermeulen@imec.be) | Van Dai Nguyen (van.dai.nguyen@imec.be)

Received: 17 April 2026 | **Revised:** 3 July 2026 | **Accepted:** 30 July 2026

Keywords: chiral coupling | Dzyaloshinskii–Moriya interaction | magnetic tunnel junction | perpendicular magnetic anisotropy | spintronic logic

ABSTRACT

Chirally coupled magnetic tunnel junctions (MTJs) have been proposed as a route toward compact spin logic architectures. Micromagnetic simulations indeed show that chiral coupling between adjacent MTJs with perpendicular magnetic anisotropy (PMA) can be achieved through an in-plane (IP) interconnection mediated by the Dzyaloshinskii–Moriya interaction, eliminating the need for current-driven domain-wall motion. Nevertheless, experimental implementation of this concept requires precise manipulation of PMA to define IP interconnections between MTJs, as well as independent control of DMI to ensure reliable coupling. Here, we introduce a hybrid free layer (HFL) stack comprising an Ir/Co bottom layer and a CoFeB/MgO top layer providing PMA. We show that ultrathin Pt insertion layers at the Ir/Co interface provide an effective means to tune the DMI without affecting PMA, enabling independent control of both properties. Finally, we develop an ion beam etching (IBE) process on a 300-mm platform that selectively suppresses the CoFeB/MgO contribution to PMA, thereby converting the stack to IP magnetization. This approach enables the manipulation of the PMA of the interconnecting free layer during MTJ patterning, providing a scalable pathway for the fabrication of chirally coupled MTJs.

1 | Introduction

As CMOS technology faces increasing scaling challenges, spintronics is being explored for alternative logic architectures. In particular, spintronic inverters and majority gates offer a compact and energy-efficient implementation [1].

A prominent pathway is current-driven domain-wall (DW) logic, where magnetic DWs are driven by spin–orbit torque (SOT) in heavy-metal/ferromagnet tracks. Logic operations based on DW motion have been demonstrated in Pt/Co stacks [2, 3]. Moreover, electrical detection and nucleation of DWs have been achieved using magnetic tunnel junctions (MTJs) based on CoFeB/MgO, which provides high tunneling magnetoresistance (TMR) and efficient spin-transfer torque (STT) [4]. Despite these advances, practical implementation of DW logic remains hindered by the need for SOT current, which introduces complex current distributions and Joule heating [1].

This is an open access article under the terms of the Creative Commons Attribution License, which permits use, distribution and reproduction in any medium, provided the original work is properly cited.
© 2026 The Author(s). *Advanced Electronic Materials* published by Wiley-VCH GmbH

Chirally coupled MTJs have been proposed by simulation as a potential approach to address the challenges of DW motion [5]. In this concept, MTJs with perpendicular magnetic anisotropy (PMA) are interconnected through an in-plane (IP) magnetized region. Interfacial Dzyaloshinskii–Moriya interaction (DMI) [6, 7] induces chiral coupling [2], resulting in antiparallel alignment of adjacent MTJs. As a result, STT-switching of the input MTJ leads to the switching of the output MTJ in the opposite direction driven by the chiral coupling. The device operation therefore relies on the interplay between PMA and DMI, enabling the implementation of compact logic gates without the need for SOT current. Nevertheless, to realize this concept experimentally, three material requirements must be met: (i) MTJ-compatibility for TMR/STT-based read/write, (ii) suitable PMA and DMI interplay to ensure reliable chiral coupling [5], and (iii) nanoscale manipulation of PMA to achieve IP interconnecting regions.

Hybrid free layer (HFL) stacks combining CoFeB/MgO with Pt/Co have been demonstrated to provide MTJ-compatibility together with high PMA and DMI in DW devices [4]. However, independent tuning of PMA and DMI is challenging as both originate from the same Pt/Co interface. Therefore, a material stack in which both properties originate from different interfaces is required. Moreover, several approaches have been demonstrated to manipulate PMA but present some limitations. He^+ ion irradiation can reduce interfacial PMA by gentle intermixing of the interfaces [8–10]. However, achieving nanoscale selectivity at wafer level with a mask approach is challenging due to the large penetration depth of light ions. Alternatively, scanning laser annealing allows local tuning of magnetic properties but is not optimal for high-throughput patterning [11]. Finally, local oxidation allows conversion from IP to PMA [2], whereas the conversion from a PMA MTJ stack to IP anisotropy is required. Hence, an industrially relevant technique on a 300-mm platform to manipulate the PMA is still needed.

In this work, we address these challenges by reengineering the HFL using low PMA Ir/Co ferromagnetically coupled with CoFeB/MgO through a W spacer. We show that in this stack design, the main PMA contribution is shifted to the top CoFeB/MgO interface, enabling independent control of PMA and DMI while preserving MTJ compatibility (see Figure 1a). We further demonstrate that ultrathin Pt insertion layers at the Ir/Co interface offer an effective means to tune DMI without impacting the PMA. Finally, we develop an ion beam etching (IBE) process that selectively suppresses the CoFeB/MgO contribution to PMA, enabling the conversion of the HFL from PMA to IP anisotropy during MTJ patterning. This novel material stack combined with the IBE treatment provides a pathway for scalable integration of chirally coupled MTJs on a 300-mm platform (see Figure 1b).

2 | Methods

2.1 | Stack Deposition

All samples were deposited using magnetron sputtering at room temperature onto thermally oxidized 300-mm Si/SiO2 wafers in a Canon–Anelva EC7800 cluster tool. Ir, Pt, Co, W and the CoFeB in the capping layer were deposited using Kr gas, while CoFeB, MgO, Mg, Ru and Ta were deposited using Ar gas. A TaN(2nm) seed

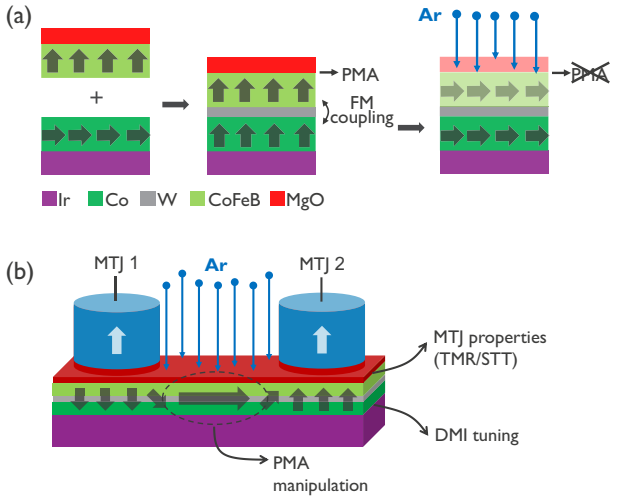


FIGURE 1 | (a) HFL stack consisting of IP magnetized Ir/Co ferromagnetically coupled with CoFeB/MgO using a W spacer. The PMA of the HFL stack is provided by the CoFeB/MgO interface. The stack can be converted from PMA to IP by selectively suppressing the PMA of the top interface using IBE. (b) Chirally coupled MTJs with the Ir/Co-based HFL stack. The CoFeB/MgO interface provides TMR and STT, while the bottom interface allows for DMI tuning. The interconnecting region is converted to IP anisotropy during MTJ patterning by IBE.

layer was used for all stacks. A wedge along the wafer is used to vary the thickness of the Co layer t_{Co}. After deposition, all wafers were annealed at 300°C for 30 min using an ASM A412 furnace.

2.2 | Magnetic Characterization

Magnetic characterization was performed using vibrating sample magnetometry (VSM, Microsense EasyVSM EV11) with 8 mm × 8 mm samples. The effective anisotropy field $\mu_0 H_k^{eff}$ is obtained by computing the area between the normalized out-of-plane (OOP) and in-plane (IP) loops as explained in Note S1. The saturation magnetization M_s and magnetic dead layer t_{dl} of Co are obtained from the slope and intercept, respectively, of the linear fit of the saturation moment m_s vs. t_{Co}, as explained in Note S2. The effective anisotropy is given by $K_{eff} = \mu_0 H_k^{eff} M_s/2$.

2.3 | Hall Bar Fabrication and Electrical Measurements

Hall bar devices with 20 μm × 200 μm channels were patterned by photolithography and ion beam etching. A second photolithography and a lift-off process were undertaken to fabricate contact electrodes consisting of Ti(20nm)/Au(500nm).

Hysteresis loop shift measurements were performed in a home-built setup with a Keithley 2602B Source and Measurement Unit to apply DC currents and measure Hall voltages.

2.4 | Brillouin Light Scattering

The Dzyaloshinskii–Moriya interaction was quantified by Brillouin Light Scattering spectroscopy (BLS) [12] using a

2199160x, 2026, 18, Downloaded from https://advanced.onlinelibrary.wiley.com/doi/10.1002/aelm.70536, Wiley Online Library on [10/11/2026]. See the Terms and Conditions (https://onlinelibrary.wiley.com/terms-and-conditions) on Wiley Online Library for rules of use; OA articles are governed by the applicable Creative Commons License

single-mode laser with wavelength $\lambda = 457$ nm and 30 mW power applied to the sample. The numerical aperture of the lens system is NA = 0.04, with a laser spot size of $\sim 20\ \mu$m. The sample was mounted in an electromagnet in Damon–Eshbach geometry on a rotatable stage, allowing the control of the angle of incidence of the laser beam. Backscattered light from the sample is collected by the same lens and analyzed using a multipass tandem Fabry–Pérot interferometer connected to a single-photon counting detector. Rotation of the sample stage by up to 90° from normal incidence allows for selective detection of spin waves with wavevectors up to ~ 25 rad/μm.

2.5 | Ion Beam Etching

Ion beam etching (IBE) was performed using a Canon–Anelva NC8000 tool with Ar ions at 200V at normal incidence with a gas flow of 20 SCCM. The IBE process was immediately followed by the in situ deposition of a 10-nm SiN encapsulation layer to protect the magnetic layers from oxidation in ambient air.

3 | Results and Discussion

3.1 | Interfacial PMA Contributions in Pt/Co- and Ir/Co-Based Hybrid Free Layers

A hybrid free layer (HFL) stack consists of a bottom heavy metal (HM)/ferromagnet (FM) layer ferromagnetically coupled with CoFeB/MgO through a W spacer providing interlayer exchange coupling [4]. The top CoFeB/MgO layer provides TMR and STT, while the bottom HM/FM layer is typically Pt/Co, providing both PMA and DMI for DW logic [10]. Nevertheless, this makes independent tuning of DMI and manipulation of PMA challenging, while it is desired for chirally coupled MTJs. To alleviate these challenges, we develop a novel HFL stack by introducing Ir/Co as bottom layer with lower PMA or even IP anisotropy. We show that the dominant PMA contribution is provided by the CoFeB/MgO interface, allowing for the manipulation of the PMA using treatments affecting the top interface, such as ion beam etching (IBE).

Figure 2a shows VSM loops for the single layer Pt(5)/Co(t_{Co})/Ru(1)/Ta(3) (thicknesses in nm) and for the HFL Pt(5)/Co(t_{Co})/W(0.3)/CoFeB(0.7)/MgO(1) with a nonmagnetic capping layer CoFeB(0.5)/Mg(0.7)/Ta(3), with $t_{Co} = 1.8$ nm. Both samples exhibit strong PMA. Figure 2b shows the effective anisotropy field $\mu_0 H_k^{eff}$ as a function of t_{Co} for both stacks. The single Pt/Co layer exhibits a wide and strong PMA window from 0.6 to 1.9 nm. Above 2 nm, shape anisotropy overcomes interfacial PMA, leading to the transition to IP anisotropy. For the HFL, the PMA window has a similar width, but the effective anisotropy field decreases by approximately a factor of two. This suggests that the PMA is mainly provided by the bottom Pt/Co interface and diluted by the CoFeB.

Figure 2c,d presents the corresponding data for Ir/Co-based stacks. In Figure 2c, we observe that the single Ir/Co layer exhibits strong IP anisotropy. Interestingly, the HFL exhibits strong PMA thanks to the CoFeB/MgO interface. In Figure 2d, the single Ir/Co layer shows a narrower PMA window (0.8-1.5 nm) and weaker anisotropy compared to Pt/Co. On the contrary, the HFL exhibits a wider PMA window (up to 1.9 nm) compared to the single layer and an effective anisotropy field roughly 200 mT higher. This reversed behavior indicates that in the Ir/Co-based HFL stack, the PMA is mainly provided by the CoFeB/MgO interface with a weaker contribution from the Ir/Co interface.

These contrasting behaviors of the two HFL stacks can be interpreted using a simplified model for the HFL effective anisotropy $K_{eff,HFL}$, derived in the Note S3. Assuming perfect ferromagnetic coupling between both layers, and ignoring a correction term for M_s mismatch, $K_{eff,HFL}$ simplifies as a thickness-weighted average of the K_{eff} of each layer, i.e. $K_{eff,HFL} = \frac{K_{eff1}t_1 + K_{eff2}t_2}{t_1+t_2}$. This model implies that $K_{eff,CoFeB} < K_{eff,PtCo}$ leads to the PMA reduction from single layer to HFL observed for Pt/Co. In contrast, for Ir/Co, $K_{eff,CoFeB} > K_{eff,IrCo}$ leads to higher PMA for the HFL than for the single layer.

These results provide key material stack design guidelines. While both stacks exhibit high TMR above 100% (see Note S4), the interfacial PMA contributions can be controlled by the choice of the heavy metal. In Pt/Co-based HFL stacks, the primary contributor to the PMA is the bottom Pt/Co interface. These stacks are therefore suited for applications, such as DW logic, requiring robust PMA of the magnetic interconnection between MTJs against fabrication processes that could affect the top interfaces [4]. Contrastingly, in Ir/Co-based HFL stacks, the top CoFeB/MgO layer is the main contributor to the PMA. Interestingly, for t_{Co} from 1.6 to 1.9 nm, the HFL has PMA while the single layer exhibits IP anisotropy. This opens new possibilities for PMA to IP conversion by selectively suppressing the PMA provided by the CoFeB/MgO using IBE, as we demonstrate in Section C. Moreover, in the next section, we show that ultrathin insertion layers allow the tuning of the DMI at the Ir/Co interface. This enables independent tuning of DMI and manipulation of PMA in an MTJ-compatible stack, as desired for chirally coupled MTJs.

3.2 | Tuning DMI Using Pt Insertion Layers

As shown in the previous section, Ir/Co-based HFL stacks are promising for PMA manipulation via the dominant CoFeB/MgO top interface. Nevertheless, the relatively low interfacial DMI of Ir/Co is limiting its direct applicability for chirally coupled MTJs. Here, we show that DMI can be effectively tuned at the Ir/Co interface without affecting PMA by inserting an ultrathin Pt layer, enabling independent control of PMA and DMI.

Interfacial DMI originates from broken inversion symmetry and strong spin–orbit coupling (SOC) in the adjacent heavy metal. It is mainly determined by the first atomic layers at the interface, with a major contribution from the SOC in the first heavy-metal atomic layer [13], and is relatively robust against interfacial intermixing [14, 15]. As a result, even ultrathin Pt insertions could significantly enhance the DMI.

In contrast, interfacial PMA at Pt/Co interfaces primarily arises from hybridization between Co 3d and Pt 5d orbitals, combined with the strong SOC of Pt [16, 17], and is highly sensitive to

2199160x, 2026, 18, Downloaded from https://advanced.onlinelibrary.wiley.com/doi/10.1002/aelm.70536, Wiley Online Library on [10/11/2026]. See the Terms and Conditions (https://onlinelibrary.wiley.com/terms-and-conditions) on Wiley Online Library for rules of use; OA articles are governed by the applicable Creative Commons License

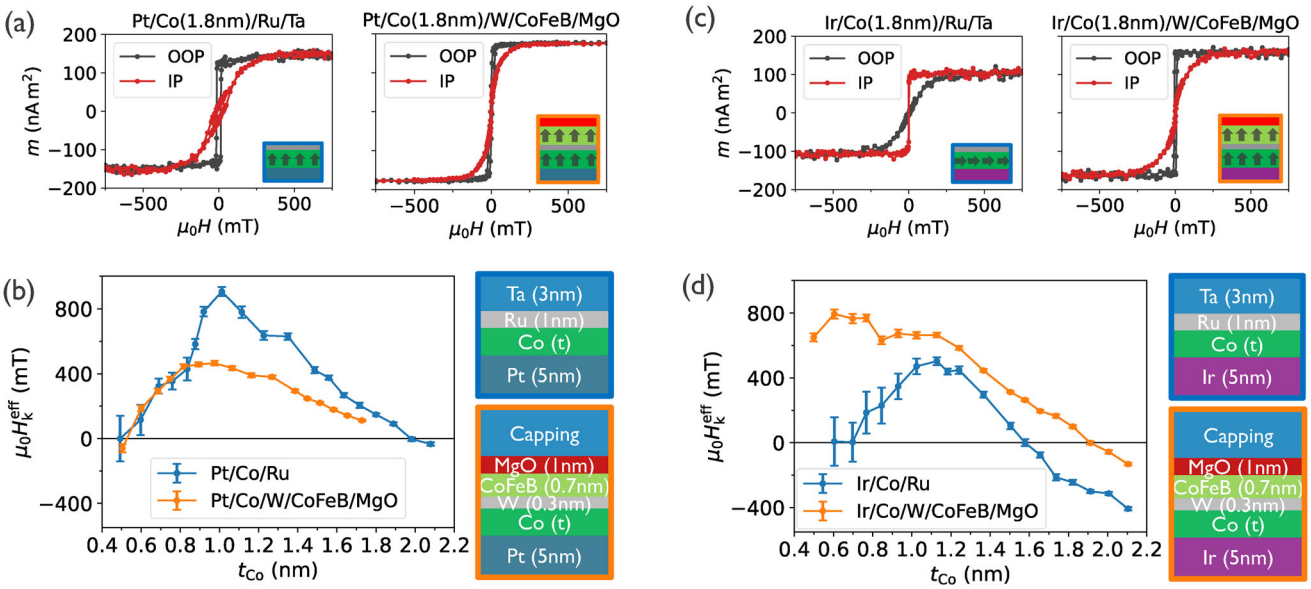


FIGURE 2 | (a) OOP and IP VSM loops for the Pt/Co single layer (left) and HFL layer (right) with $t_{Co} = 1.8$ nm. (b) Effective anisotropy field $\mu_0 H_k^{eff}$ as a function of Co thickness for the Pt/Co single layer and HFL stacks (see schematics of the stacks). (c) OOP and IP VSM loops for the Ir/Co single layer (left) and HFL layer (right) with $t_{Co} = 1.8$ nm. (d) Effective anisotropy field $\mu_0 H_k^{eff}$ as a function of Co thickness for the Ir/Co single layer and HFL stacks (see schematics of the stacks).

interface quality and chemical ordering [18]. Consequently, the potential enhancement of PMA by ultrathin Pt insertions is expected to be weaker than that of DMI.

In this section, we first show that Pt insertion layers at the Ir/Co interface have limited impact on the interfacial PMA, and then demonstrate a significant enhancement of DMI.

3.2.1 | Impact of Pt Insertion on PMA

To evaluate the effect of Pt insertion layers at the Ir/Co interface, we deposited Ir(5)/Pt(t_{Pt})/Co(t_{Co})/Ru(1)/Ta(3) samples with $t_{Pt} = 0$, 0.1, 0.2, 0.3 nm and t_{Co} varying along a wedge (see Figure 3a).

Figure 3b shows that the magnetic dead layer t_{dl} slightly decreases with increasing Pt insertion, which we attribute to the proximity-induced magnetism in Pt [19–23] and changes in interface quality. The effective anisotropy field $\mu_0 H_k^{eff}$ as a function of Co thickness t_{Co} for the different Pt insertions is presented in Figure 3c. Remarkably, the overall profile of $\mu_0 H_k^{eff}$ remains nearly unchanged for different Pt insertion thicknesses, and remains considerably lower than for Pt/Co/Ru. The onset of the PMA window is only slightly shifted, consistent with the trend in the dead layer thickness. To further elucidate the impact on interfacial PMA, we extract the interfacial contribution K_t using the intercept of a linear fit of the relation $K_{eff} t_{eff} = K_t + \left(K_B - \frac{\mu_0 M_s^2}{2}\right) t_{eff}$ (see Note S2) [24, 25], where $t_{eff} = t_{Co} - t_{dl}$ is the effective thickness and K_B is the bulk contribution. Figure 3d shows that the Pt insertion layers have no significant impact on the interfacial anisotropy K_t, which remains consistently lower than the value for Pt/Co. Little impact on the total volume contributions is also obtained in Note S2.

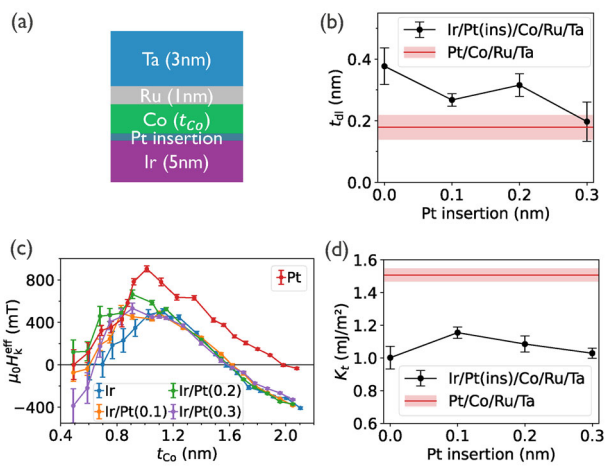


FIGURE 3 | (a) Schematic of the stack with Pt insertion layers at the Ir/Co interface. (b) Magnetic dead layer thickness as a function of Pt insertion layer thickness. (c) Effective anisotropy field $\mu_0 H_k^{eff}$ as a function of Co thickness for different Pt insertion layer thicknesses. (d) Interfacial anisotropy constant K_t as a function Pt insertion layer thickness. The horizontal solid lines and shaded areas correspond to the values/error bars for Pt/Co/Ru.

These results confirm that ultrathin Pt insertion layers have minimal impact on the interfacial PMA, opening the door for independent tuning of DMI.

3.2.2 | DMI Quantification by Hysteresis Loop Shift

To evaluate the impact of Pt insertion layers on the DMI, we fabricated Hall bar devices with a 20-μm-wide channel (see Methods) for Ir(5)/Pt(t_{Pt})/Co(1.2)/Ru(1)/Ta(3) stacks with $t_{Pt} = 0$,

2199160x, 2026, 18, Downloaded from https://advanced.onlinelibrary.wiley.com/doi/10.1002/aelm.70536, Wiley Online Library on [10/11/2026]. See the Terms and Conditions (https://onlinelibrary.wiley.com/terms-and-conditions) on Wiley Online Library for rules of use; OA articles are governed by the applicable Creative Commons License

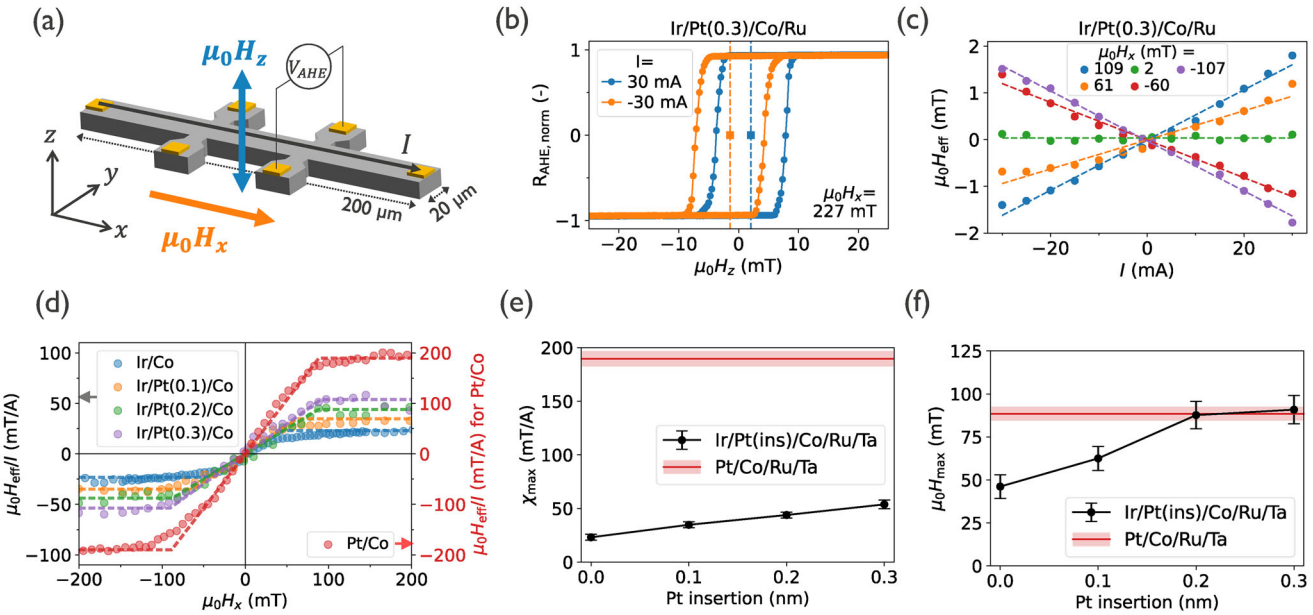


FIGURE 4 | (a) Schematic of a Hall bar device for hysteresis loop shift measurement. (b) AHE loop for Ir/Pt(0.3)/Co(1.2)/Ru for dc currents $I = \pm 30$ mA and an in-plane bias field $\mu_0 H_x = 227$ mT. (c) $\mu_0 H_{eff}$ for Ir/ Pt(0.3)/Co(1.2)/Ru as a function of dc current under different in-plane bias fields. (d) $\mu_0 H_{eff}/I$ as a function of in-plane field for Ir/Pt(t_{Pt})/Co(1.2)/Ru and Pt/Co(1.2)/Ru. (e,f) $\mu_0 H_{eff}/I$ at saturation (e) and saturation field $\mu_0 H_{max}$ (f) as a function of Pt insertion layer thickness. The horizontal solid lines and shaded areas correspond to the values/error bars for Pt/Co(1.2)/Ru.

0.1, 0.2, 0.3 nm. The DMI and SOT effective field were quantified by the hysteresis loop shift method [26], as illustrated in Figure 4a. A DC current I is applied in the channel along the x direction and the anomalous Hall effect (AHE) voltage V_{AHE} is measured in the y direction, while sweeping an OOP field $\mu_0 H_z$ and applying a fixed IP bias field $\mu_0 H_x$. Well-defined DW nucleation centers were created in the channel close to the electrodes, as described in the Note S5.

Figure 4b shows representative normalized AHE loops for $t_{Pt} =$ 0.3 nm with $\mu_0 H_x = 150$ mT and $I = \pm 30$ mA. The opposite loop shifts along the $\mu_0 H_z$ axis for opposite polarities of I allow the extraction of the SOT effective field $\mu_0 H_{eff}$. Figure 4c shows representative measurements of $\mu_0 H_{eff}$ vs. I for different IP fields. The excellent linear relationship between $\mu_0 H_{eff}$ and I, together with opposite slopes for opposite IP fields and the absence of $\mu_0 H_{eff}$ for zero IP field, is consistent with conventional SOT-driven DW motion. The corresponding plots for every sample are shown in Note S6.

Figure 4d shows the SOT effective field per unit current $\mu_0 H_{eff}/I$ as a function of IP field, for the different Pt insertion thicknesses as well as a reference Pt/Co sample. For all samples, $\mu_0 H_{eff}/I$ increases quasi-linearly with $\mu_0 H_x$ and saturates at $\mu_0 H_{max}$. The DMI field $\mu_0 H_{DMI}$ can be computed using $\mu_0 H_{DMI} = \mu_0 H_{max} - \mu_0 H_S$ where $\mu_0 H_S$ is the DW anisotropy field. $\mu_0 H_S$ is approximated to 25 mT for all samples [27]. The DMI coefficient D can then be computed with $D = \mu_0 H_{DMI} \Delta M_s$ [28, 29] where $\Delta = \sqrt{A_{ex}/K_{eff}}$ is the DW parameter with $A_{ex} \sim 13$ pJ/m the exchange stiffness [30] (see Note S8).

Figure 4e,f summarizes the extracted $\mu_0 H_{eff}/I$ at saturation (denoted χ_{max}) and $\mu_0 H_{max}$ as a function of Pt insertion thickness. The small increase in χ_{max} is attributed to the Pt insertion improving spin Hall effect (SHE) and Rashba–Edelstein effect (REE) [31], while the SHE in the Ir remains low compared to Pt. In contrast, the drastic enhancement in $\mu_0 H_{max}$, reaching values comparable with Pt/Co, indicates a strong enhancement of DMI. This finding is consistent with the interfacial origin of DMI, which arises from SOC in the first atomic layers of the heavy metal. Therefore, even ultrathin layers of Pt significantly boost the DMI.

These results reveal that ultrathin Pt insertion at the Ir/Co provides a powerful means to tune DMI without significantly impacting PMA. In comparison, the insertion of ultrathin Ir at a Pt/Co interface [32] leads to a drastic decrease of the DMI without significant impact on PMA and SOT efficiency, as reported in Note S7 [32].

3.2.3 | DMI Quantification by BLS

To validate the DMI enhancement observed from hysteresis loop shift measurements, we performed Brillouin Light Scattering (BLS) spectroscopy (see Methods) [12, 24, 33–35] on samples with different Pt insertion thicknesses. A slightly larger Co thickness of 1.6 nm was selected to reduce PMA and facilitate the BLS measurement.

In the Damon–Eshbach geometry [12], an external field $\mu_0 H_x$ sets the magnetization direction in-plane, perpendicular to the detected spin-wave propagation direction, as illustrated in the inset of Figure 5a. The laser incidence angle θ selects the detected magnon wavevector $|k| = 4\pi \sin\theta/\lambda$ with λ the laser wavelength. The corresponding frequency shift f_{shift} of backscattered light due to the magnon interaction is then recorded.

2199160x, 2026, 18, Downloaded from https://advanced.onlinelibrary.wiley.com/doi/10.1002/aelm.70536, Wiley Online Library on [10/11/2026]. See the Terms and Conditions (https://onlinelibrary.wiley.com/terms-and-conditions) on Wiley Online Library for rules of use; OA articles are governed by the applicable Creative Commons License

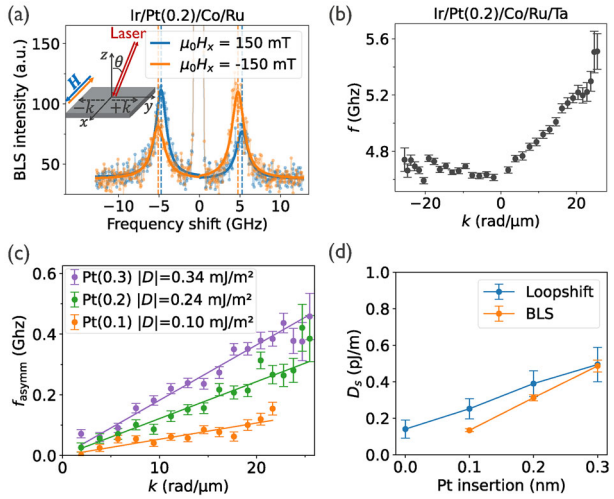


FIGURE 5 | (a) Representative BLS spectrum for Ir/Pt(0.2)/Co(1.6)/Ru for $|k| = 19.1$ rad/μm and $\mu_0 H_x = \pm 150$ mT. The inset is a schematic of the measurement geometry. (b) Spin wave dispersion relation for Ir/Pt(0.2)/Co(1.6)/Ru. (c) Asymmetric part of the dispersion relation and fit for different Pt insertion layer thicknesses. (d) Interfacial DMI coefficient D_s as a function of Pt insertion layer thickness, extracted from BLS and hysteresis loop shift measurements.

A representative BLS spectrum is shown in Figure 5a for $\theta = 44°$ (i.e. $|k| \sim 19.1$ rad/μm). The peaks at negative (positive) f_{shift} correspond to creation (annihilation) of magnons by Stokes (anti-Stokes) processes [12, 36]. The peaks are fitted with a Lorentzian function to extract the magnon frequencies f. To remove instrumental asymmetries, we averaged the Stokes frequency at $\mu_0 H_x < 0$ and the anti-Stokes frequency at $\mu_0 H_x > 0$ to define $f(k > 0)$, and vice versa for $f(k < 0)$. A resulting magnon dispersion relation $f(k)$ is shown in Figure 5b, where the asymmetry between positive and negative k reflects the presence of DMI.

To extract the DMI coefficient D, the asymmetric part $f_{\text{asym}}(k) = (f(+k) - f(-k))/2$ of the dispersion relation is fitted using $f_{\text{asym}}(k) = \frac{\gamma}{\pi M_s} Dk$, where $\gamma \sim 189$ GHz/T is the gyromagnetic ratio (for g factor of ~ 2.15 for fcc Co [37–41]). Besides, the fitting of the symmetric part (see Note S8) yields an exchange stiffness $A_{\text{ex}} \sim 13$ pJ/m. Figure 5c shows a linear dependence of f_{asym} on k for all samples, enabling accurate extraction of D. The increasing slope of f_{asym} vs. k for increasing t_{Pt} indicates an enhancement of the DMI. Figure 5d shows the interfacial DMI coefficient $D_s = D\, t_{\text{Co,eff}}$ as a function of t_{Pt} obtained from BLS and from hysteresis loop shift. Both methods show excellent agreement, confirming a significant increase of interfacial DMI with Pt insertion.

These results confirm that ultrathin Pt insertions at the Ir/Co interface allow the tuning of the interfacial DMI without impacting the PMA.

3.3 | PMA-to-IP Conversion by Ion Beam Etching

The Ir/Co-based HFL stack developed above, with PMA originating from the top interface, is well-suited for independent tuning of DMI at the bottom Ir/Co interface and PMA manipulation at the top CoFeB/MgO interface, as desired for chirally coupled MTJs. Here, to manipulate the PMA and achieve the conversion from PMA to IP, we employ an ion beam etching (IBE) process, an industry-standard technique widely used for MTJ fabrication. By selecting a Co thickness between 1.6 and 1.9 nm, and precisely stopping the etch on the MgO layer, we demonstrate that the PMA from the top interface can be selectively suppressed, converting the stack from PMA to IP anisotropy (as illustrated in Figure 1a).

Energy-dispersive spectroscopy (EDS) images before and after IBE until the MgO layer (41 sec) for $t_{\text{Co}} = 1.8$ nm are shown in Figure 6a,b. The images confirm that the capping layer CoFeB(0.5)/Mg(0.7)/Ta(3) was completely removed and the etch stopped on the MgO layer. The lower Mg signal indicates partial damage to the MgO layer while the CoFeB layer underneath is preserved. The EDS line profiles are provided in Note S9. Figure 6c,d shows the corresponding VSM measurements before and after IBE. Initially, the HFL stack exhibits effective PMA with $\mu_0 H_k^{\text{eff}} = 140$ mT. After IBE, the sample switched to IP anisotropy with $\mu_0 H_k^{\text{eff}} = -180$ mT, in line with the value for single Ir/Co layer, and demonstrating successful PMA-to-IP conversion.

The time evolution of the effective anisotropy field $\mu_0 H_k^{\text{eff}}$ and magnetic moment m_s during etching for different t_{Co} is shown in Figure 6e,f. Optical Emission Spectroscopy (OES) traces obtained during the IBE are provided in Note S10. Four distinct phases are identified and schematically illustrated in Figure 6g:

- A – Capping layer etching (0–30 s): the capping layer is etched without affecting the magnetic layer.
- B – PMA-to-IP conversion (30–38 s): the etching is approaching the MgO layer. The penetration depth of ~1 nm of the Ar ions allows altering the CoFeB/MgO interface while the MgO is not being etched yet. A drastic reduction of PMA is observed with a conversion to IP anisotropy for the different t_{Co}. Interestingly, the slight reduction in m_s indicates limited damage to the magnetic materials.
- C – Conversion to single layer (~41 s): the PMA of the CoFeB/MgO is completely suppressed, and the stack exhibits strong IP anisotropy matching the properties of the Ir/Co single layer (plotted as dashed lines).
- D – Over-etching (>41 s): the magnetic layers are progressively etched, leading to a strong reduction of m_s, decreased thickness and loss of the IP anisotropy.

These results demonstrate that IBE allows the manipulation of the magnetic anisotropy in HFL stacks. In particular, $t_{\text{Co}} = 1.8$ nm exhibits a conversion from strong PMA to strong IP anisotropy.

Importantly, the consistent magnetic behavior observed across repeated etching times confirms the reproducibility of the IBE process. Moreover, the use of a 300-mm industrial platform, together with previous demonstrations of wafer-level uniformity for similar stacks [4], supports its scalability and uniformity.

Therefore, this method offers a promising avenue toward the fabrication of chirally coupled MTJs, where the interconnections are converted to IP anisotropy during the MTJ patterning by IBE, as illustrated in Figure 1b. Since the IBE is localized to the exposed

2199160x, 2026, 18, Downloaded from https://advanced.onlinelibrary.wiley.com/doi/10.1002/aelm.70536, Wiley Online Library on [10/11/2026]. See the Terms and Conditions (https://onlinelibrary.wiley.com/terms-and-conditions) on Wiley Online Library for rules of use; OA articles are governed by the applicable Creative Commons License

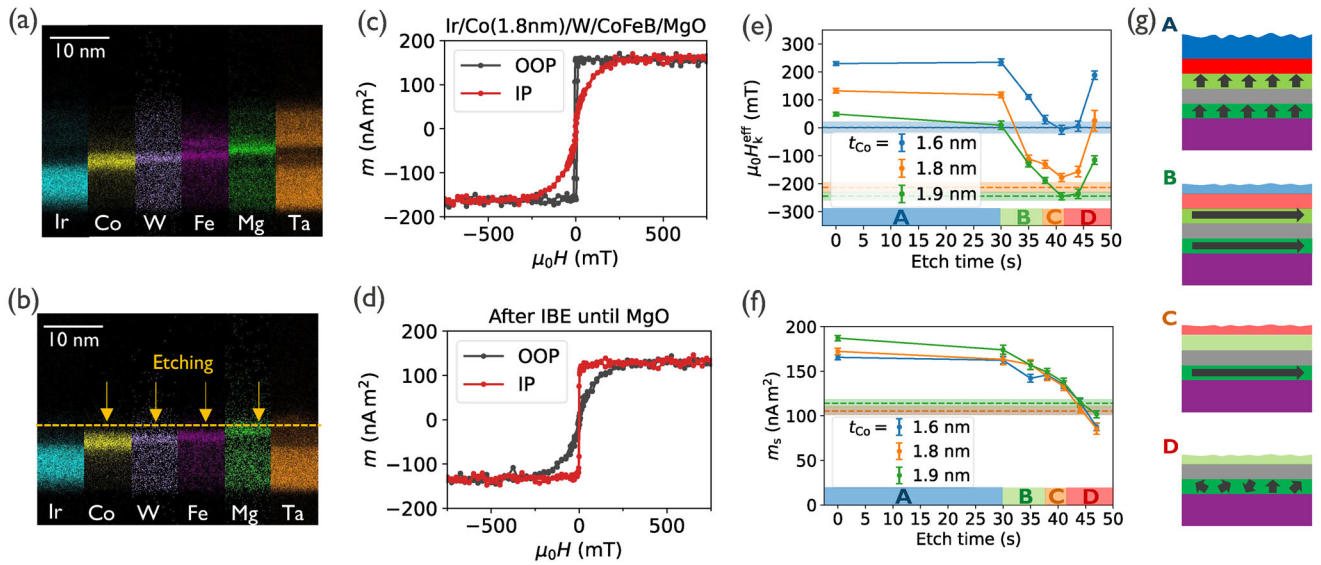


FIGURE 6 | (a,b) Individual elemental EDS slices (a) before and (b) after IBE etching until MgO (41 sec) for $t_{Co} = 1.8$ nm. (c,d) OOP and IP VSM loops (c) before and (d) after IBE etching until MgO (41 sec) for $t_{Co} = 1.8$ nm. (e,f) Time evolution of the effective anisotropy field $\mu_0 H_k^{eff}$ and magnetic moment m_s during etching for different t_{Co}. The dashed lines and shaded areas correspond to the values and error bars for the Ir/Co/Ru/Ta single layer with the same t_{Co}. (g) Schematics of the stack during the etching.

interconnection regions, the MgO barrier within the MTJ pillars is expected to remain intact, thereby preserving the TMR [4, 42].

Combined with the DMI tuning strategy using Pt insertions, this approach provides a scalable pathway for the integration of spintronic logic devices on a 300-mm platform.

4 | Conclusions

In summary, we established an approach that enables independent control of Dzyaloshinskii–Moriya interaction (DMI) and perpendicular magnetic anisotropy (PMA) in hybrid free layer (HFL) stacks for chirally coupled MTJs.

First, by comparing Pt/Co- and Ir/Co-based HFL stacks, we identified how the choice of heavy metal determines the dominant source of PMA. We showed that in Ir/Co-based stacks, the PMA is mainly provided by the top CoFeB/MgO interface.

Second, we demonstrated that ultrathin Pt insertion layers at the Ir/Co interface strongly enhance the DMI without major impact on the interfacial PMA.

Finally, we developed a 300-mm compatible ion beam etching (IBE) process that selectively suppresses the CoFeB/MgO contribution to PMA. This process enables the conversion from PMA to IP anisotropy during MTJ patterning.

The integration of the proposed heterostructures into practical devices is supported by prior demonstrations of similar HFL stacks exhibiting excellent thermal stability and endurance in MRAM devices [43–45]. Furthermore, related domain-wall and multipillar SOT devices have been realized with sub-80-nm MTJ dimensions [4, 42], highlighting the feasibility of integration into nanoscale device geometries.

Together, these results provide a scalable pathway for implementing chirally coupled MTJs, opening opportunities for compact spintronic logic architectures.

Acknowledgements

This work has been enabled in part by the NanoIC pilot line. The acquisition and operation are jointly funded by the Chips Joint Undertaking, through the European Union's Digital Europe (101183266) and Horizon Europe programs (101183277), as well as by the participating states Belgium (Flanders), France, Germany, Finland, Ireland and Romania. For more information, visit nanoic-project.eu. B.V. acknowledges FWO-Vlaanderen for a Strategic Basic Research PhD fellowship No. 1S72225N. B. V. thanks Florin Ciubotaru (imec) for facilitating the collaboration with RPTU University Kaiserslautern–Landau for the BLS measurements. This research was funded by the European Research Council within the Starting Grant No. 101042439 "CoSpiN". D.G. acknowledges FWO-Vlaanderen for a Strategic Basic Research PhD fellowship No. 1SHEV24N. K.T. acknowledges the KU Leuven C14/24/110 program and the FWO-FNRS Weave program G0D7723N-FWO. S. S. was supported by the MOTIE (Ministry of Trade, Industry, and Energy) in Korea, under the Fostering Global Talents for Innovative Growth Program (P0017312) supervised by the Korea Institute for Advancement of Technology (KIAT).

Conflicts of Interest

The authors declare no conflicts of interest.

Data Availability Statement

The data that support the findings of this study are available from the corresponding author upon reasonable request.

References

1. B. B. Vermeulen, B. Sorée, S. Couet, K. Temst, and V. D. Nguyen, "Progress in Spin Logic Devices Based on Domain-Wall Motion," *Micromachines* 15, no. 6 (2024): 696, https://doi.org/10.3390/mi15060696.

2199160x, 2026, 18, Downloaded from https://advanced.onlinelibrary.wiley.com/doi/10.1002/aelm.70536, Wiley Online Library on [10/11/2026]. See the Terms and Conditions (https://onlinelibrary.wiley.com/terms-and-conditions) on Wiley Online Library for rules of use; OA articles are governed by the applicable Creative Commons License

2. Z. Luo, T. P. Dao, A. Hrabec, et al., "Chirally Coupled Nanomagnets," *Science* 363, no. 6434 (2019): 1435–1439, https://doi.org/10.1126/science.aau7913.

3. Z. Luo, A. Hrabec, T. P. Dao, et al., "Current-Driven Magnetic Domain-Wall Logic," *Nature* 579, no. 7798 (2020): 214–218, https://doi.org/10.1038/s41586-020-2061-y.

4. E. Raymenants, O. Bultynck, D. Wan, et al., "Nanoscale Domain Wall Devices with Magnetic Tunnel Junction Read and Write," *Nature Electronics* 4, no. 6 (2021): 392–398, https://doi.org/10.1038/s41928-021-00593-x.

5. B. B. Vermeulen, M. Gama Monteiro, D. Giuliano, et al., "Magnetization-Switching Dynamics Driven by Chiral Coupling," *Physical Review Applied* 21, no. 2 (2024): 024050, https://doi.org/10.1103/physrevapplied.21.024050.

6. I. Dzyaloshinsky, "A Thermodynamic Theory of "Weak" Ferromagnetism of Antiferromagnetics," *Journal of Physics and Chemistry of Solids* 4, no. 4 (1958): 241–255, https://doi.org/10.1016/0022-3697(58)90076-3.

7. T. Moriya, "Anisotropic Superexchange Interaction and Weak Ferromagnetism," *Physical Review* 120 (1960): 91–98, https://doi.org/10.1103/PhysRev.120.91.

8. C. Chappert, H. Bernas, J. Ferré, et al., "Planar Patterned Magnetic Media Obtained by Ion Irradiation," *Science* 280, no. 5371 (1998): 1919–1922, https://doi.org/10.1126/science.280.5371.1919.

9. T. Devolder, J. Ferré, C. Chappert, H. Bernas, J.-P. Jamet, and V. Mathet, "Magnetic Properties of He^{+}-Irradiated Pt/Co/Pt Ultrathin Films," *Physical Review B* 64, no. 6 (2001): 064415, https://doi.org/10.1103/physrevb.64.064415.

10. B. B. Vermeulen, E. Raymenants, V. T. Pham, et al., "Towards Fully Electrically Controlled Domain-Wall Logic," *AIP Advances* 14, no. 2 (2024): 025030, https://doi.org/10.1063/9.0000811.

11. L. J. Riddiford, J. A. Brock, K. Murawska, et al., "Two-Dimensional Gradients in Magnetic Properties Created with Direct-Write Laser Annealing," *Nature Communications* 16, no. 1 (2025): 10979, https://doi.org/10.1038/s41467-025-65921-7.

12. G. Carlotti and G. Gubbiotti, "Brillouin Scattering and Magnetic Excitations in Layered Structures," *La Rivista del Nuovo Cimento* 22, no. 12 (1999): 1–60, https://doi.org/10.1007/bf02872273.

13. H. Yang, A. Thiaville, S. Rohart, A. Fert, and M. Chshiev, "Anatomy of Dzyaloshinskii-Moriya Interaction at Co/Pt Interfaces," *Physical Review Letters* 115 (2015): 267210, https://doi.org/10.1103/PhysRevLett.115.267210.

14. B. Zimmermann, W. Legrand, D. Maccariello, et al., "Dzyaloshinskii-Moriya Interaction at Disordered Interfaces from Ab Initio Theory: Robustness Against Intermixing and Tunability Through Dusting," *Applied Physics Letters* 113, no. 23 (2018): 232403, https://doi.org/10.1063/1.5049876.

15. H. T. Nembach, E. Jué, K. Poetzger, J. Fassbender, T. J. Silva, and J. M. Shaw, "Tuning of the Dzyaloshinskii–Moriya Interaction by He+ Ion Irradiation," *Journal of Applied Physics* 131, no. 14 (2022): 143901, https://doi.org/10.1063/5.0080523.

16. N. Nakajima, T. Koide, T. Shidara, et al., "Perpendicular Magnetic Anisotropy Caused by Interfacial Hybridization via Enhanced Orbital Moment in Co/Pt Multilayers: Magnetic Circular X-Ray Dichroism Study," *Physical Review Letters* 81 (1998): 5229–5232, https://doi.org/10.1103/PhysRevLett.81.5229.

17. B. Dieny and M. Chshiev, "Perpendicular Magnetic Anisotropy at Transition Metal/Oxide Interfaces and Applications," *Reviews of Modern Physics* 89 (2017): 025008, https://doi.org/10.1103/RevModPhys.89.025008.

18. M. Bersweiler, K. Dumesnil, D. Lacour, and M. Hehn, "Impact of Buffer Layer and Pt Thickness on the Interface Structure and Magnetic Properties in (Co/Pt) Multilayers," *Journal of Physics: Condensed Matter* 28, no. 33 (2016): 336005, https://doi.org/10.1088/0953-8984/28/33/336005.

19. G. Schütz, S. Stähler, M. Knülle, P. Fischer, S. Parkin, and H. Ebert, "Distribution of Magnetic Moments in Co/Pt and Co/Pt/Ir/Pt Multilayers Detected by Magnetic X-Ray Absorption," *Journal of Applied Physics* 73, no. 10 (1993): 6430–6432, https://doi.org/10.1063/1.352622.

20. W. J. Antel, M. M. Schwickert, T. Lin, W. L. O'Brien, and G. R. Harp, "Induced Ferromagnetism and Anisotropy of Pt Layers in Fe/Pt(001) Multilayers," *Physical Review B* 60 (1999): 12933–12940, https://doi.org/10.1103/PhysRevB.60.12933.

21. F. Wilhelm, P. Poulopoulos, G. Ceballos, et al., "Layer-Resolved Magnetic Moments in Ni/Pt Multilayers," *Physical Review Letters* 85 (2000): 413–416, https://doi.org/10.1103/PhysRevLett.85.413.

22. R. M. Rowan-Robinson, A. A. Stashkevich, Y. Roussign'e, et al., "The Interfacial Nature of Proximity-Induced Magnetism and the Dzyaloshinskii-Moriya Interaction at the Pt/Co Interface," *Scientific Reports* 7, no. 1 (2017): 16835, https://doi.org/10.1038/s41598-017-17137-z.

23. A. Moskaltsova, J. Krieft, D. Graulich, T. Matalla-Wagner, and T. Kuschel, "Impact of the Magnetic Proximity Effect in Pt on the Total Magnetic Moment of Pt/Co/Ta Trilayers Studied by X-Ray Resonant Magnetic Reflectivity," *AIP Advances* 10, no. 1 (2020): 015154, https://doi.org/10.1063/1.5130031.

24. Z. Chi, Y.-C. Lau, V. L. Zhang, et al., "Relationship Between Orbital Moment Anisotropy, Magnetocrystalline Anisotropy, and Dzyaloshinskii-Moriya Interaction in W/Co/Pt Trilayers," *Physical Review B* 110 (2024): 184401, https://doi.org/10.1103/PhysRevB.110.184401.

25. R. J. J. Lim, T. S. Suraj, A. Kumar, et al., "Benchmarking Interfacial Magnetic Interactions and Spin Hall Angle in Heavy Metal /CoFeB/MgO Heterostructures," *APL Materials* 13, no. 12 (2025): 121104, https://doi.org/10.1063/5.0289920.

26. C.-F. Pai, M. Mann, A. J. Tan, and G. S. D. Beach, "Determination of Spin Torque Efficiencies in Heterostructures with Perpendicular Magnetic Anisotropy," *Physical Review B* 93 (2016): 144409, https://doi.org/10.1103/PhysRevB.93.144409.

27. T. Dohi, S. Fukami, and H. Ohno, "Influence of Domain Wall Anisotropy on the Current-Induced Hysteresis Loop Shift for Quantification of the Dzyaloshinskii-Moriya Interaction," *Physical Review B* 103 (2021): 214450, https://doi.org/10.1103/PhysRevB.103.214450.

28. A. Thiaville, S. Rohart, E. Ju'e, V. Cros, and A. Fert, "Dynamics of Dzyaloshinskii Domain Walls in Ultrathin Magnetic Films," *European Physical Journal Plus* 100, no. 5 (2012): 57002, https://doi.org/10.1209/0295-5075/100/57002.

29. S. Emori, U. Bauer, S.-M. Ahn, E. Martinez, and G. S. D. Beach, "Current-Driven Dynamics of Chiral Ferromagnetic Domain Walls," *Nature Materials* 12, no. 7 (2013): 611–616, https://doi.org/10.1038/nmat3675.

30. C. Eyrich, W. Huttema, M. Arora, et al., "Exchange Stiffness in Thin Film Co Alloys," *Journal of Applied Physics* 111, no. 7 (2012): 07C919, https://doi.org/10.1063/1.3679433.

31. D. Kumar, T. Jin, R. Sbiaa, et al., "Domain Wall Memory: Physics, Materials, and Devices," *Physics Reports* 958 (2022): 1–35, https://doi.org/10.1016/j.physrep.2022.02.001.

32. H. Fan, Z. Shao, J. Wang, et al., "Elucidating the Role of an Ir Insertion Layer in Mediating Interfacial Perpendicular Anisotropy, Dzyaloshinskii-Moriya Interaction, and Spin-Orbit Torque in Pt/Ir/Co," *Physical Review B* 108 (2023): 224409, https://doi.org/10.1103/PhysRevB.108.224409.

33. M. Belmeguenai, M. S. Gabor, Y. Roussign'e, et al., "Brillouin Light Scattering Investigation of the Thickness Dependence of Dzyaloshinskii-Moriya Interaction in Co ∗ 0.5Fe ∗ 0.5 Ultrathin Films," *Physical Review B* 93 (2016): 174407, https://doi.org/10.1103/PhysRevB.93.174407.

34. T. Böttcher, T. S. Suraj, X. Chen, et al., "Quantifying Symmetric Exchange in Ultrathin Ferromagnetic Films with Chirality," *Physical Review B* 107 (2023): 094405, https://doi.org/10.1103/PhysRevB.107.094405.

35. T. Bottcher, K. Lee, F. Heussner, et al., "Heisenberg Exchange and Dzyaloshinskii–Moriya Interaction in Ultrathin Pt(W)/CoFeB Single and

2199160x, 2026, 18, Downloaded from https://advanced.onlinelibrary.wiley.com/doi/10.1002/aelm.70536, Wiley Online Library on [10/11/2026]. See the Terms and Conditions (https://onlinelibrary.wiley.com/terms-and-conditions) on Wiley Online Library for rules of use; OA articles are governed by the applicable Creative Commons License

Multilayers," *IEEE Transactions on Magnetics* 57, no. 7 (2021): 1–7, https://doi.org/10.1109/tmag.2021.3079259.

36. M. Kuepferling, A. Casiraghi, G. Soares, et al., "Measuring Interfacial Dzyaloshinskii-Moriya Interaction in Ultrathin Magnetic Films," *Reviews of Modern Physics* 95 (2023): 015003, https://doi.org/10.1103/RevModPhys.95.015003.

37. B. Heinrich, J. F. Cochran, M. Kowalewski, et al., "Magnetic Anisotropies and Exchange Coupling in Ultrathin fcc Co(001) Structures," *Physical Review B* 44 (1991): 9348–9361, https://doi.org/10.1103/PhysRevB.44.9348.

38. J. Pelzl, R. Meckenstock, D. Spoddig, F. Schreiber, J. Pflaum, and Z. Frait, "Spin–Orbit-Coupling Effects on g-Value and Damping Factor of the Ferromagnetic Resonance in Co and Fe Films," *Journal of Physics: Condensed Matter* 15, no. 5 (2003): S451, https://doi.org/10.1088/0953-8984/15/5/302.

39. M. A. W. Schoen, J. Lucassen, H. T. Nembach, et al., "Magnetic Properties of Ultrathin 3*d* Transition-Metal Binary Alloys. I. Spin and Orbital Moments, Anisotropy, and Confirmation of Slater-Pauling Behavior," *Physical Review B* 95 (2017): 134410, https://doi.org/10.1103/PhysRevB.95.134410.

40. M. Belmeguenai, J.-P. Adam, Y. Roussign'e, et al., "Interfacial Dzyaloshinskii-Moriya Interaction in Perpendicularly Magnetized Pt/Co/AlO_x Ultrathin Films Measured by Brillouin Light Spectroscopy," *Physical Review B* 91 (2015): 180405, https://doi.org/10.1103/PhysRevB.91.180405.

41. M. Belmeguenai, Y. Roussign'e, S. M. Ch'erif, et al., "Influence of the Capping Layer Material on the Interfacial Dzyaloshinskii–Moriya Interaction in Pt/Co/Capping Layer Structures Probed by Brillouin Light Scattering," *Journal of Physics D: Applied Physics* 52, no. 12 (2019): 125002, https://doi.org/10.1088/1361-6463/aafdf5.

42. K. Cai, S. Van Beek, S. Rao, et al., "Selective Operations of Multi-Pillar SOT-MRAM for High Density and Low Power Embedded Memories," in *2022 VLSI Technology and Circuits*, (2022), 375–376.

43. E. Liu, J. Swerts, Y. C. Wu, et al., "Top-Pinned STT-MRAM Devices with High Thermal Stability Hybrid Free Layers for High-Density Memory Applications," *IEEE Transactions on Magnetics* 54, no. 11 (2018): 1–5, https://doi.org/10.1109/TMAG.2018.2831904.

44. S. Couet, S. Rao, S. Van Beek, et al., "BEOL Compatible High Retention Perpendicular SOT-MRAM Device for SRAM Replacement and Machine Learning," in *2021 Symposium on VLSI Technology* (IEEE, 2021), 1–2.

45. S. Van Beek, K. Cai, F. Yasin, et al., "Scaling the SOT Track – A Path Towards Maximizing Efficiency in SOT-MRAM," in *2023 International Electron Devices Meeting (IEDM)* (IEEE, 2023), 1–4.

Supporting Information

Additional supporting information can be found online in the Supporting Information section.

Supporting File: aelm70536-sup-0001-SuppMat.pdf.

2199160x, 2026, 18, Downloaded from https://advanced.onlinelibrary.wiley.com/doi/10.1002/aelm.70536, Wiley Online Library on [10/11/2026]. See the Terms and Conditions (https://onlinelibrary.wiley.com/terms-and-conditions) on Wiley Online Library for rules of use; OA articles are governed by the applicable Creative Commons License